



1     Improving the Confidence in Retrievals of Vertical Distributions of Cloud Condensation Nuclei  
2             Number Concentration from ARM Supported by Aircraft In Situ Observations  
3  
4     Jingjing Tian, Gourihar Kulkarni, Jennifer M. Comstock, John E. Shilling, Damao Zhang, Peng  
5             Wu, and Fan Mei  
6  
7             Pacific Northwest National Laboratory, Richland, Washington  
8  
9             Corresponding author: Jingjing Tian ([jingjingtian5@gmail.com](mailto:jingjingtian5@gmail.com))  
10



11 **Abstract:** Accurate quantification of the vertical distribution of cloud condensation nuclei (CCN)  
12 number concentrations is critical for improving our understanding of aerosol–cloud interactions.  
13 Ground-based Raman lidars operated by the Atmospheric Radiation Measurement (ARM)  
14 program, together with surface CCN measurements, are used to retrieve vertically resolved CCN  
15 number concentrations (Retrieved Number concentration of CCN, RNCCN). These retrievals rely  
16 on several assumptions, including that aerosol composition is vertically homogeneous. To assess  
17 this assumption, we developed and tested a framework to infer the dominant aerosol classes/types  
18 at different altitudes. This was done by applying a k-Nearest-Neighbors (kNN) algorithm to lidar  
19 ratio and linear depolarization ratio measurements from Raman lidar. We evaluated the framework  
20 using aircraft aerosol and CCN measurements from the ARM Holistic Interactions of Shallow  
21 Clouds, Aerosols, and Land Ecosystems (HI-SCALE) field campaign. The results show that  
22 RNCCN performance degrades as vertical aerosol complexity increases, i.e., RNCCN agrees with  
23 the aircraft CCN in vertically homogeneous conditions, but closure decreases in layered aerosol  
24 structures. To generalize beyond individual examples, we introduce a metric (heterogeneity index)  
25 that quantifies the vertical complexity by assessing the variation of inferred aerosol classes/types.  
26 Case-level statistics show a tendency for RNCCN and aircraft differences to increase with this  
27 metric. By detecting retrievals that are likely compromised by aerosol vertical heterogeneity, the  
28 proposed framework improves the interpretability and effective use of RNCCN used for long-term  
29 evaluation of models and aerosol–cloud interactions.

30

31

32

33

34



## 35 1. Introduction

36 Aerosol particles in the atmosphere that serve as cloud condensation nuclei (CCN) are  
37 critical to the formation of clouds and influence cloud optical properties and cloud life cycle,  
38 thereby affecting the Earth's energy balance and hydrological cycle (Lohmann and Feichter, 2005;  
39 Rosenfeld et al., 2014; Dong et al., 2015; Bellouin et al., 2020). These CCN-driven changes in  
40 cloud properties are central to aerosol–cloud interactions (ACI) and contribute to aerosol indirect  
41 radiative forcing, whose magnitude remains one of the largest uncertainties in Earth system model  
42 simulations (Gryspeerd et al., 2023).

43 Accurately quantifying ACI critically depends on understanding the vertical distribution of  
44 CCN. Ground-based CCN measurements alone are insufficient, as they cannot capture these  
45 variations with altitude. In particular, CCN in the sub-cloud layer approaching cloud base directly  
46 influence the initial number of cloud droplets and subsequent microphysical processes.  
47 Consequently, the ability of Earth system models to reliably simulate cloud droplet activation and  
48 assess aerosol indirect effects is contingent on the accurate representation of these vertical CCN  
49 profiles (e.g., Ghan et al., 2012; Watson-Parris et al., 2019).

50 Considering the scarcity of in situ aircraft measurements of CCN vertical profiles, lidar  
51 observations provide a crucial source of information. Various methods have been developed to  
52 retrieve CCN concentrations from spaceborne (satellite) and ground-based lidar observations.  
53 Satellite lidar products, such as aerosol backscatter, extinction, and aerosol type information, are  
54 widely used to estimate CCN profiles through modeling and empirical relationships (e.g.,  
55 Choudhury and Tesche, 2022b, a; Kapustin et al., 2006; Kulkarni et al., 2025). These estimates  
56 complement traditional satellite-derived aerosol products and enable global-scale estimates of  
57 CCN (e.g., Shinozuka et al., 2015; Levy et al., 2013).

58 Ground-based lidar approaches offer higher vertical resolution and have been widely used  
59 in CCN retrievals. For example, polarization lidar is combined with AERONET data to classify  
60 aerosol types and derive empirical relationships between extinction coefficients and dry particle  
61 size thresholds, enabling the estimation of CCN number concentrations (Mamouri and Ansmann,  
62 2016). A multi-wavelength lidar inversion technique has been applied to retrieve aerosol size  
63 distributions from optical properties, thereby estimating CCN concentrations (Lv et al., 2018).  
64 More recently, the empirical regression method has been used to directly relate lidar extinction to  
65 collocated in situ CCN measurements, mainly for biomass aerosols, offering improved accuracy  
66 for ground-based CCN retrievals (Lenhardt et al., 2023).

67 In contrast to the above type-dependent or inversion-based approaches, “extinction-based”  
68 methods estimate CCN profiles by combining vertically resolved lidar extinction with a near-  
69 surface CCN constraint, avoiding the need for multi-wavelength microphysical inversions or  
70 aerosol-type-specific parameterizations. This provides a computationally simple and operationally  
71 robust pathway for continuous CCN profiling when only standard lidar products are available  
72 (Shinozuka et al., 2015; Lenhardt et al., 2023; Ghan et al., 2006). Specifically, Ghan et al. (2004)  
73 derived CCN number concentration profiles by scaling surface CCN measurements using  
74 vertically resolved aerosol extinction from Raman lidar, enabling application at sites with routine



75 surface CCN observations and standard lidar observations. The U.S. Department of Energy's  
76 Atmospheric Radiation Measurement (ARM) user facility developed the Retrieved Number  
77 Concentration of CCN (RNCCN) product based on this methodology (Kulkarni et al., 2023),  
78 enabling continuous estimation of CCN number concentration (Brendecke et al., 2022; Kulkarni  
79 et al., 2025).

80 One of the underlying assumptions within the RNCCN calculation is that aerosol properties  
81 (e.g., type, shape) are vertically uniform (i.e., invariant with height). However, this assumption  
82 could be invalid, especially when heterogeneous aerosol layers aloft are observed (e.g., Clarke et  
83 al., 1997; Fast et al., 2022; Russell et al., 2014; Seinfeld et al., 2016). Consequently, evaluating  
84 RNCCN requires explicitly identifying conditions where aerosol properties vary or remain  
85 invariant with height. We hypothesize that deviations from the vertical uniformity assumption of  
86 aerosol properties may lead to systematic discrepancies between RNCCN and in situ CCN (e.g.,  
87 with large errors expected under more vertically heterogeneous aerosol conditions). To test this  
88 hypothesis, we need to have 1) a method to diagnose vertical aerosol heterogeneity from available  
89 remote-sensing observables and 2) in situ CCN data that can be used to quantify how such  
90 heterogeneity impacts RNCCN accuracy.

91 Aerosol properties' vertical heterogeneity can be inferred through variations in aerosol  
92 optical properties. Lidar measurements offer a powerful tool for detecting and characterizing these  
93 variations (Ferrare et al., 2023; Groß et al., 2025; Müller et al., 2007; Omar et al., 2009;  
94 Papagiannopoulos et al., 2018; Sugimoto et al., 2002). Two key lidar-derived parameters, linear  
95 depolarization ratio (LDR) and lidar ratio (LR), provide insight into aerosol shape, composition,  
96 and size. The LDR distinguishes spherical particles (e.g., pollution, smoke) from non-spherical  
97 ones (e.g., dust, ash), while the LR reflects differences in aerosol composition and size distribution  
98 (Burton et al., 2012; Groß et al., 2015; Müller et al., 2007). Recent advances in machine learning  
99 (ML) offer the potential for more automated and robust aerosol classification from lidar  
100 observations, particularly when multi-wavelength or fluorescence capabilities are available  
101 (Nicolae et al., 2018; Veselovskii et al., 2022). Such ML frameworks typically depend on  
102 specialized instrumentation and often require synthetic training datasets or site-specific tuning,  
103 which may limit their broader applicability. These limitations pose difficulties for applying  
104 existing ML methods to a specific lidar (e.g., the DOE ARM Raman lidar), which operates at a  
105 single wavelength (355 nm) and lacks fluorescence detection. To address this gap, we need to  
106 develop a new classification/cluster approach tailored to a single-wavelength Raman lidar.

107 High-quality in situ data from both surface and aircraft collected by the DOE ARM  
108 program provide an opportunity for us to investigate whether vertical heterogeneity in aerosol  
109 properties (e.g., type, shape, or composition) impacts the reliability of RNCCN retrievals. The  
110 Holistic Interactions of Shallow Clouds, Aerosols, and Land Ecosystems (HI-SCALE) field  
111 campaign, conducted in spring and summer 2016 near the SGP Central Facility, deployed research  
112 aircraft to collect vertically resolved CCN and aerosol measurements across a range of land surface  
113 types (Fast et al., 2019). Using this dataset, it has been found that the extinction-based RNCCN  
114 method outperforms satellite- and model-based estimates in reproducing airborne CCN



115 observations (Kulkarni et al., 2025). Building upon this understanding and complementing this  
116 finding, our study focuses on identifying and quantifying conditions, particularly vertically  
117 heterogeneous aerosol structures diagnosed from lidar observables, under which RNCCN retrieval  
118 confidence may be reduced.

119 This study introduces a framework to relate vertical heterogeneity in aerosol optical  
120 properties to RNCCN error. We test the hypothesis that vertically heterogeneous (layered) aerosol  
121 conditions, diagnosed by height-dependent variations in lidar ratio and linear depolarization ratio,  
122 produce larger CCN retrieval errors than vertically homogeneous (well-mixed) aerosol layers. To  
123 validate this, we compare CCN profiles retrieved using the standard RNCCN assumption of  
124 vertically uniform aerosol properties against in situ aircraft measurements and quantify how  
125 retrieval errors vary as the diagnosed heterogeneity increases.

## 126 **2. Data**

127 This study uses multi-platform ARM observations to develop and evaluate an aerosol type  
128 classification framework. Aerosol types are classified based on the DeLiAn (**D**epolarization ratio,  
129 **L**idar ratio, and **Å**ngström exponent, details in section 2.1) database using ARM Raman lidar (RL)  
130 observations (section 2.2). The RNCCN (section 2.3) is compared with G-1 aircraft CCN  
131 measurements (section 2.4) to test the hypothesis.

### 132 **2.1 Aerosol Type Database**

133 The DeLiAn database (Floutsi et al., 2023) is utilized in this study because it provides the  
134 comprehensive aerosol optical properties needed to develop an aerosol classification framework.  
135 To our knowledge, DeLiAn is one of the most extensive and up-to-date datasets for aerosol typing  
136 for ground-based lidar, making it invaluable for aerosol classification tasks. Its data and  
137 classifications have been widely used to inform aerosol schemes for the EarthCARE mission  
138 (Wandinger et al., 2023) and satellite-based algorithms, such as CALIPSO's aerosol subtype  
139 classification (Kim et al., 2018; Tackett et al., 2023).

140 The DeLiAn database compiles lidar parameters (LDR and LR), and aerosol optical  
141 properties (Ångström exponent) from ground-based Raman and polarization lidars operated at 355,  
142 532, and 1064 nm. Values are typically derived in cloud-free conditions and represent aerosol  
143 layers identified within the lowest few kilometers of the troposphere, where the ground-based  
144 lidars provide the most reliable aerosol retrievals. The database includes 13 aerosol classes. These  
145 consist of seven pure types (clean marine, dried marine, pollution, continental background,  
146 tropospheric smoke, stratospheric smoke, and regional dust from Saharan, Central Asian, and  
147 Middle Eastern sources) and six common mixtures involving dust combined with smoke,  
148 pollution, or marine aerosols. These measurements are conducted by the Leibniz Institute for  
149 Tropospheric Research (TROPOS) using advanced lidar systems (Engelmann et al., 2016)  
150 deployed at fixed EARLINET sites (Pappalardo et al., 2014) and mobile platforms, including ship-  
151 based campaigns (Bohlmann et al., 2018; Engelmann et al., 2021; Kanitz et al., 2013). The data  
152 span diverse geographic regions, including Europe, the Middle East, Central Asia, North Africa,  
153 and marine environments.



154 This study uses the DeLiAn dataset, specifically the aerosol-types inferred from the lidar  
155 parameters (LR and LDR) and their reported uncertainties (i.e., the reported standard deviations  
156 reflecting layer-averaging, instrument noise, and calibration uncertainty) at 355 nm. We use the  
157 355 nm subset because it matches the wavelength of the ARM Raman lidar used to generate the  
158 RNCCN product.

## 159 2.2 ARM Raman Lidar

160 ARM RL observations from the Southern Great Plains (SGP) site are used. The RL  
161 provides vertical measurements of aerosol backscatter, extinction, LR, and LDR at 355 nm  
162 wavelength at 30-meter vertical and 2-minute temporal resolutions. The dataset is available  
163 through the Raman Lidar Profiles-Feature detection and Extinction (RLPROF-FEX) Value-Added  
164 Product (VAP) (Thorsen et al., 2015a, 2015b; Chand et al., 2019).

## 165 2.3 ARM CCN Vertical Profile

166 To estimate vertical CCN concentrations, this study uses the RNCCN VAP developed by  
167 DOE ARM (Kulkarni et al., 2023; Kulkarni et al., 2025), based on the method developed by Ghan  
168 and Collins (2004) and Ghan et al. (2006). This VAP provides vertical profiles of CCN  
169 concentration at 10-minute temporal resolution and 60-meter vertical resolution, by scaling surface  
170 CCN measurements using dry-corrected aerosol extinction profiles (also provided within RNCCN  
171 VAP), which are derived from Raman lidar observations. The RNCCN concentration at a given  
172 height  $z$ , time  $t$ , and supersaturation  $SS$  is calculated as:

$$173 \text{RNCCN}(z, t, SS) = \text{CCN}(0, t, SS) \times [\alpha_{\text{dry}}(z, t) / \alpha_{\text{dry}}(0, t)] \quad (1)$$

174 where  $\text{CCN}(0, t, SS)$  is the surface CCN concentration, and  $\alpha_{\text{dry}}(z, t)$  and  $\alpha_{\text{dry}}(0, t)$  are the dry-  
175 corrected aerosol extinction values at height  $z$  and the surface, respectively.

176 Surface-based CCN measurements at various supersaturation values are obtained from the  
177 DOE ARM dual-column CCN-200 instrument (Uin and Enekwizu, 2024). The instrument reports  
178 CCN number concentrations as a function of supersaturation, at 1 Hz resolution. During standard  
179 operation, the instrument cycles through six supersaturation levels per hour, ranging from 0 to  
180 1.0%, with each level maintained for several minutes.

181 The dry extinction profile is computed by adjusting the ambient extinction profile from  
182 RLPROF-FEX using a relative humidity (RH)-dependent aerosol humidification factor,  $f(\text{RH})$ ,  
183 parameterized with a gamma coefficient ( $\gamma$ ) that reflects the sensitivity of extinction to RH  
184 (Dawson et al., 2020; Zieger et al., 2010). The gamma value is empirically derived for each day  
185 from collocated extinction and RH profiles. This correction ensures that the extinction profile  
186 reflects dry aerosol conditions, which are more directly related to the CCN measurements.

187 Various quality control tests are applied to generate the RNCCN dataset. RL profiles with  
188 missing RH and aerosol mask features are excluded (Kulkarni et al., 2025). RH profiles that exceed  
189 85% are omitted to avoid large, highly uncertain hygroscopic-growth corrections and potential  
190 cloud/near-saturation contamination. Temperature profiles (Newsom et al., 2018a, b) that report  
191 supercooled temperatures are also excluded because mixed-phase/cloud contamination can bias



192 the Raman retrievals and the associated extinction-to-CCN scaling. These filters reduce data  
193 availability during some cold-season periods, but do not eliminate wintertime RNCCN retrievals  
194 overall. Further, extinction profiles are also filtered using feature masks (Chand et al., 2019;  
195 Thorsen et al., 2015; Thorsen and Fu, 2015) to remove cloud and precipitation layers. RNCCN can  
196 still be retrieved in aerosol-only regions below cloud base; however, profiles (or portions of  
197 profiles) flagged as precipitation are excluded because the mask is no longer classified as aerosol,  
198 and reliable extinction retrievals are not available. Because of high uncertainty from the  
199 instrument's near-field overlap, the extinction values at the lowest measurement level, the first  
200 range gate (i.e., the first discrete altitude interval above the ground where the lidar returns are  
201 processed), can be larger than  $0.4 \text{ km}^{-1}$  or below  $0.02 \text{ km}^{-1}$  (Kulkarni et al., 2025). When the first  
202 range gate extinction falls within the acceptable range ( $0.02\text{--}0.4 \text{ km}^{-1}$ ), it is used because it is  
203 closest to the surface CCN measurement and best represents the near-surface aerosol used to  
204 anchor the scaling. When it falls outside this range, the extinction value from the second range  
205 gate is used for RNCCN estimation.

#### 206 **2.4 ARM G1 Aircraft data**

207 We used in situ CCN measurements collected during the 2016 HI-SCALE campaign near  
208 the SGP site. The aircraft sampled vertical aerosol and meteorological profiles, with CCN  
209 concentrations measured at 1 Hz using a dual-column CCN counter operating at fixed  
210 supersaturations of 0.24% and 0.46% (Uin and Mei, 2019). We focused on the 0.24% channel to  
211 compare with extinction-based RNCCN estimates because the activation dry diameters  
212 corresponding to this SS contributed significantly to the extinction (Kulkarni et al., 2025). Only  
213 data obtained under cloud-free conditions were used. The high temporal and vertical resolution of  
214 the G-1 data, averaged to 10-minute intervals, provided a benchmark for evaluating RNCCN  
215 retrieval uncertainty.

### 216 **3. Methodology**

#### 217 **3.1 k-Nearest Neighbors: Model Configuration and Training**

218 We used a kNN classifier to map Raman-lidar observations into aerosol-type classes  
219 defined in the DeLiAn database. The classifier was implemented in Python using scikit-learn  
220 (KNeighborsClassifier; Pedregosa et al., 2011). kNN is a versatile algorithm and requires only a  
221 few user-specified parameters, primarily the number of neighbors ( $k$ ) and a distance metric,  
222 making it straightforward to implement in this study. As a non-parametric ML method, it does not  
223 impose a predefined functional form on the decision boundary (i.e., the surface in feature space  
224 that separates different aerosol/CCN regimes). Instead, it learns this boundary directly from the  
225 data, which allows it to capture nonlinear relationships and still perform robustly with relatively  
226 small training datasets, making it a practical choice for this study.

227 The kNN method is implemented using LDR and LR as input features. For each new  
228 observation, kNN searches the DeLiAn database for the  $k$  most similar samples (i.e., closest in the  
229 LDR–LR feature space) and assigns the aerosol type based on the majority class among those

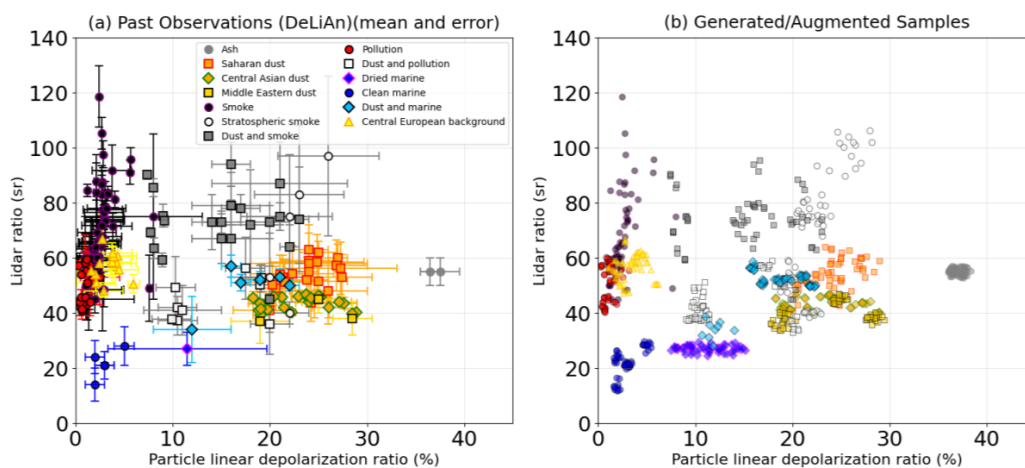


230 nearest neighbors. The development of our kNN classifier involved three key stages with careful  
231 design: (A) curating the source dataset, (B) augmenting the data to create a balanced training set,  
232 and finally (C) training and optimizing the model. These stages are discussed as follows.

233 (A) To adapt the kNN model for the continental SGP site, we refined the standard DeLiAn  
234 training dataset by curating its “marine” aerosol class. The default DeLiAn marine  
235 definition ( $LDR < 5\%$ ,  $LR \approx 30\text{--}40$  sr) overlaps strongly with SGP pollution and would  
236 tend to misclassify pollution as marine despite typically weak marine influence at SGP  
237 (Liu et al., 2021). Moreover, field observations indicate that typical marine aerosols  
238 exhibit very low depolarization ( $< 3\%$ ) and lower LR ( $\sim 20\text{--}25$  sr) (Groß et al., 2017,  
239 2025; Illingworth et al., 2015). We find that the anomalously high LR values in the  
240 DeLiAn marine class are mainly associated with rare shipborne “dried-marine” cases  
241 from cruise, where sea-salt particles are modified by dry free-tropospheric air (Haarig  
242 et al., 2017). Thus, we excluded these non-representative cruise samples to improve  
243 climatological consistency and reduce misclassification. After filtering, the remaining  
244 DeLiAn “marine” class mainly occupies the low-LDR/low-LR corner.

245 (B) The DeLiAn database (Floutsi et al., 2023) based aerosol types are shown in Figure 1a.  
246 Here, the aerosol-type classification is performed using paired measurements of LDR  
247 (%) and LR (steradian, sr) at 355 nm. Several aerosol types in the DeLiAn database  
248 contain only a small number of observations. To prevent these sparsely sampled classes  
249 from being overwhelmed by well-sampled types in the kNN voting step, we apply an  
250 uncertainty-aware augmentation procedure. For each observation, synthetic samples  
251 are generated by perturbing LDR and LR within their reported measurement  
252 uncertainties, using a truncated range to avoid unrealistic values. We then balance the  
253 training set by expanding each aerosol type to 61 samples, the size of the largest well-  
254 sampled class in the original DeLiAn dataset (Smoke; 61 valid observations). All other  
255 classes are augmented to this size (Figure 1b), ensuring comparable representation  
256 across aerosol types without oversampling beyond the existing majority class.

257 (C) During training, LDR and LR are standardized using statistics from the augmented  
258 dataset (i.e., the DeLiAn observations plus the uncertainty-perturbed synthetic  
259 samples). We use a kNN classifier with Euclidean distance and distance-weighted  
260 voting (i.e., closer neighbors receive higher weights in the class assignment), chosen  
261 for its non-parametric nature and its ability to represent the locally clustered structure  
262 of aerosol types in LDR–LR space. The number of neighbors ( $k$ ) is selected via 5-fold  
263 stratified cross-validation, where augmentation and scaling are performed within each  
264 training fold. The value of  $k$  with the highest mean macro-averaged F1 score (a standard  
265 metric that balances precision and recall across all classes) is used in all subsequent  
266 analyses. Final model training is performed on the full augmented dataset and LDR–  
267 LR observations that are standardized and classified using this trained model.



268

269 Figure 1. (a) DeLiAn aerosol linear depolarization ratio vs. lidar ratio observations at 355 nm  
 270 showing the original measured points with their reported uncertainties (error bars) (reproduced  
 271 using data in Floutsi et al., 2023). (b) Training dataset after uncertainty-aware augmentation: each  
 272 original observation is supplemented by synthetic samples generated by perturbing LDR and LR  
 273 within the reported uncertainties, so that each aerosol type contains 61 samples. Colors denote the  
 274 13 aerosol types.

### 275 3.2 ML Model Performance

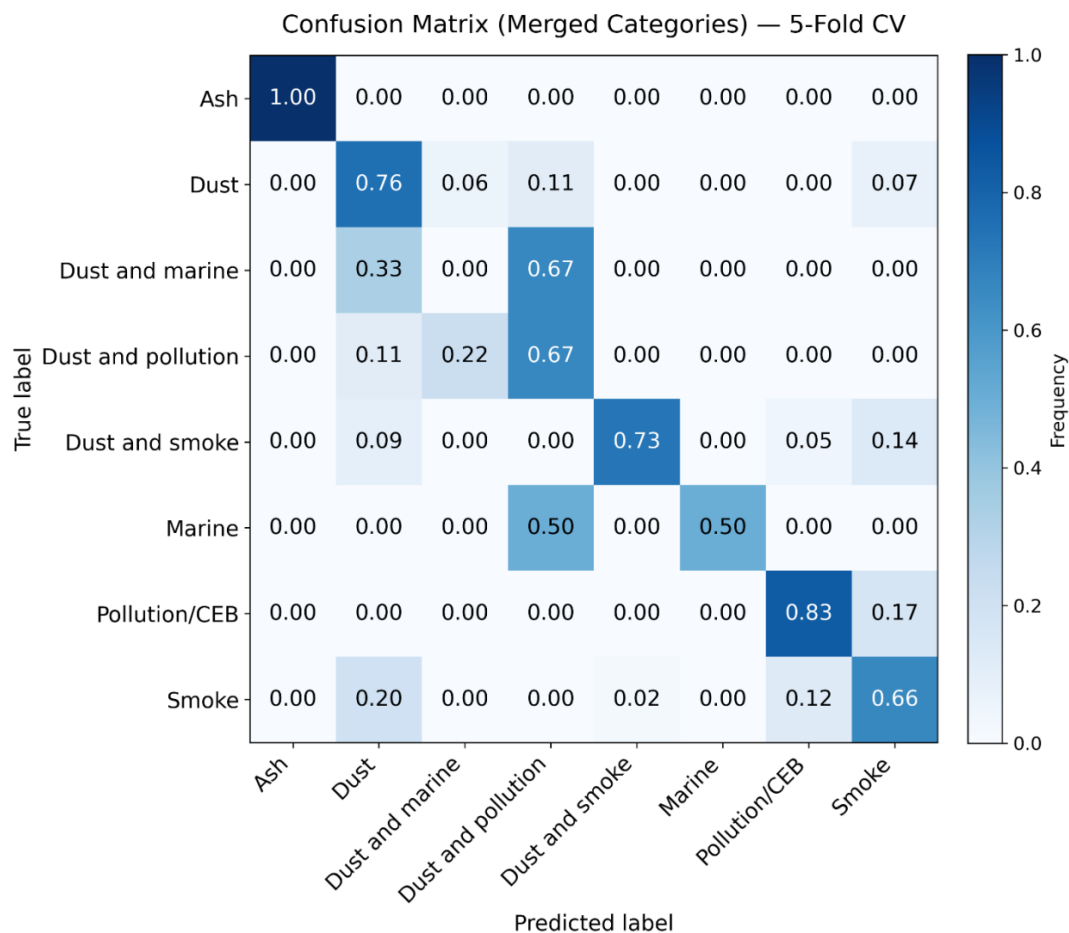
276 The kNN classifier’s performance was assessed using 5-fold stratified cross-validation. For  
 277 each fold, the training data portion was independently augmented using the uncertainty-aware  
 278 procedure described in Section 3.1. This standard practice ensures that the model is always  
 279 evaluated on held-out data untouched by the augmentation process. Predictions for each test fold  
 280 were then collected and aggregated to generate the final performance metrics.

281 The resulting row-normalized confusion matrix is shown in Figure 2. Each row  
 282 corresponds to the true aerosol class and each column to the predicted class; values indicate the  
 283 fraction of samples in a true class assigned to each predicted class. Darker diagonal elements  
 284 indicate more accurate classifications, while off-diagonal elements highlight systematic confusion  
 285 between classes.

286 We merged aerosol classes into broader categories to improve the interpretability of the  
 287 confusion matrix while preserving dominant optical similarities. Specifically, Marine combines  
 288 Clean marine and Dried marine; Dust combines Saharan dust, Central Asian dust, and Middle  
 289 Eastern dust; Pollution/Central European Background (CEB) combines Pollution and Central  
 290 European background, because the CEB type largely represents aged continental anthropogenic  
 291 aerosol, it is also grouped with pollution in the final aerosol classification; and Smoke combines  
 292 Smoke and Stratospheric smoke. All other categories (Ash, Dust and smoke, Dust and pollution,  
 293 Dust and marine) remain unchanged.



294           The confusion matrix is shown in Figure 2. Classification performance is type dependent  
295 and is constrained by the use of only two lidar observables (LR and LDR). Optically distinct  
296 classes are retrieved with high fidelity: “Ash” is classified perfectly (1.00), and key fine-mode  
297 anthropogenic regimes are well resolved, including Pollution/CEB (0.83) and Smoke (0.66). In  
298 contrast, ambiguity increases among dust and mixed classes with overlapping LDR–LR signatures.  
299 For example, “Dust and marine” is frequently confused with “Dust” (0.33) and “Dust and  
300 pollution” (0.67). “Dust and pollution” is split between its correct label (0.67), “Dust and marine”  
301 (0.22), with the remaining fraction assigned to “Dust” (0.11). This is consistent with the limited  
302 separability of mixtures using only two optical features. Higher-fidelity discrimination would  
303 require additional independent observables (e.g., multiwavelength backscatter/extinction or  
304 spectral depolarization), which is beyond the scope of this LR–LDR-only framework. Importantly,  
305 most misclassifications occur among closely related dust/mixed categories that occupy similar  
306 regions of LR–LDR space, rather than between fundamentally different regimes. Because our  
307 application is to diagnose vertical heterogeneity and layer structure, not to provide definitive  
308 aerosol composition, the classifier skill should be sufficient for identifying transitions between  
309 distinct optical regimes.  
310



311

312 Figure 2. Row-normalized confusion matrix for the kNN aerosol-type classifier using merged  
 313 DeLiAn categories, based on 5-fold stratified cross-validation. Rows denote the true class, and  
 314 columns denote the predicted class; diagonal elements give the per-class recall (classification  
 315 accuracy), and off-diagonal elements show the fraction misclassified into other classes. The  
 316 corresponding confusion matrix for the original (unmerged) DeLiAn classes is shown in Appendix  
 317 Figure A.

318 In addition, this kNN-based framework assumes that the major aerosol types encountered  
 319 at SGP are reasonably represented in the DeLiAn training set and that Raman-lidar LR and LDR  
 320 provide meaningful signatures for separating those types. As with any lidar-based typing approach,  
 321 uncertainties arise from the instruments' calibration drift and low-SNR conditions, which can  
 322 reduce classification confidence. Because kNN assigns types based on similarity in LR–LDR  
 323 space, mixed aerosol and observations near class boundaries may occasionally blur distinctions  
 324 among categories. Accordingly, the inferred types should be interpreted as an optical-regime



325 diagnostic rather than a definitive statement of aerosol composition. This caveat is important to  
326 keep in mind when interpreting RNCCN behavior under complex or heterogeneous aerosol  
327 conditions.

## 328 **4. Results and Discussions**

### 329 **4.1 Case-Based Evaluation of RNCCN**

330 In this section, we first focus on case studies from HI-SCALE periods when in situ CCN  
331 measurements and RNCCN retrievals are available. To ensure comparability, we selected cases  
332 where (1) the G1 remained within 100 km (radially) of the Raman lidar site and (2) the aircraft  
333 operated below the planetary boundary layer height (PBLH; Zhang et al., 2022). These cases  
334 enable a very detailed examination of how aerosol type classification helps interpret differences  
335 between aircraft in situ CCN measurements and retrieved RNCCN values. For case analysis, we  
336 selected three flight days (3, 11, and 17 September 2016) to show more details. These cases  
337 (summarized in Table 1) span a range of aerosol conditions from vertically homogeneous (case  
338 #1) to highly heterogeneous (case #3), with case #2 in between.

#### 339 **4.1.1 Case #1: Vertically Relative Homogeneous Pollution**

340 Figure 3 presents a case from 11 September 2016 characterized by relatively stable aerosol  
341 properties and limited vertical variability in LDR and LR over the 15:10–18:10 UTC. The time–  
342 height evolution of LDR (Figure 3a) shows consistently low values (<2%), while LR (Figure 3b)  
343 remains mostly between 30 and 60 sr. In the DeLiAn database (Figure 1a), this region of LDR–  
344 LR space is dominated by pollution aerosols; our ML model also identified this period as pollution  
345 (Figure 3c).

346 The comparison between retrieved RNCCN and in situ CCN concentrations is shown in  
347 Figure 3d. During 15:40–16:50 UTC (between the dashed lines), when the G-1 aircraft remained  
348 within ~30 km of the Raman lidar, RNCCN agrees closely with the aircraft CCN measurements.  
349 This distance threshold (30 km) is chosen because the RNCCN product is averaged over 10-minute  
350 intervals, during which the aircraft typically travels about 60 km at ~100 m s<sup>-1</sup>; a 30 km radius  
351 therefore approximates the spatial footprint of the lidar retrieval. Within this 30 km radial vicinity,  
352 the mean aircraft CCN concentration is 367 cm<sup>-3</sup>, and the collocated RNCCN retrievals have a  
353 mean value of 386 cm<sup>-3</sup>, an RMSE of 97 cm<sup>-3</sup>, and a small positive bias of ~19 cm<sup>-3</sup> (Table 1).  
354 This indicates a slight systematic overestimation of CCN by RNCCN under well-collocated,  
355 vertically homogeneous conditions.

356 In contrast, surface CCN measurements (orange squares) are substantially higher than both  
357 RNCCN and aircraft CCN, often by roughly a factor of two. This behavior demonstrates that  
358 near-surface CCN concentrations are not always representative of CCN aloft, even during  
359 relatively uniform aerosol conditions.

360 Even as the aircraft distance from the Raman lidar increases later in the period (red curve  
361 in Figure 3d), RNCCN remains broadly consistent with the in-situ measurements, indicating  
362 horizontal homogeneity in aerosol type and loading in this case. Overall, Case #1 represents a near-



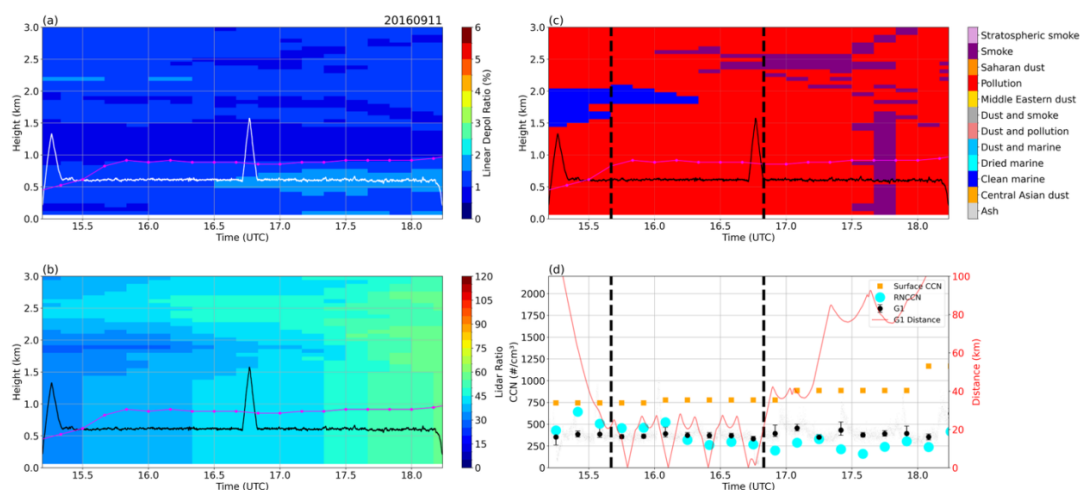
363 ideal condition/scenario for applying the RNCCN method: a stable aerosol with minimal vertical  
 364 structure and high classification confidence, resulting in comparatively low CCN retrieval  
 365 uncertainty compared to aircraft measurements.

366 Table 1. Summary of RNCCN performance for the three HI-SCALE case days

Date	Key features	Mean aircraft CCN (cm <sup>-3</sup> )	Mean Surface CCN (cm <sup>-3</sup> )	Mean RNCCN (cm <sup>-3</sup> )	RMSE (RNCCN vs. aircraft) (cm <sup>-3</sup> )
Case #1 2016-09-11	Vertically homogeneous aerosol	367	765	386	97
Case #2 2016-09-17	Moderate heterogeneity with mixed aerosol types	560	1019	614	373
Case #3 2016-09-03	Large heterogeneity with strongly layered aerosols	899	1859	1600	1276

367

368



369

370 Figure 3. Time–height cross sections on 11 September 2016 (Case #1): (a) LDR (%) from Raman  
 371 lidar, with the white line showing G-1 aircraft altitude and magenta line the planetary boundary  
 372 layer height from Doppler lidar; (b) same as (a), but for lidar ratio (sr); (c) aerosol type  
 373 classification from the kNN model; (d) time series of in situ CCN concentration aboard the G-1 at  
 374 0.24% supersaturation (black circles: median, with 25–75% interquartile range), overlaid with  
 375 collocated RNCCN retrievals (cyan circles) and surface CCN (orange squares). The red line (right  
 376 axis) shows aircraft distance from the SGP Raman lidar; vertical dashed lines indicate the period  
 377 when the aircraft was within ~30 km of the site.

378 **4.1.2 Case #2: Moderately Heterogeneous, Mixed Aerosol Types**

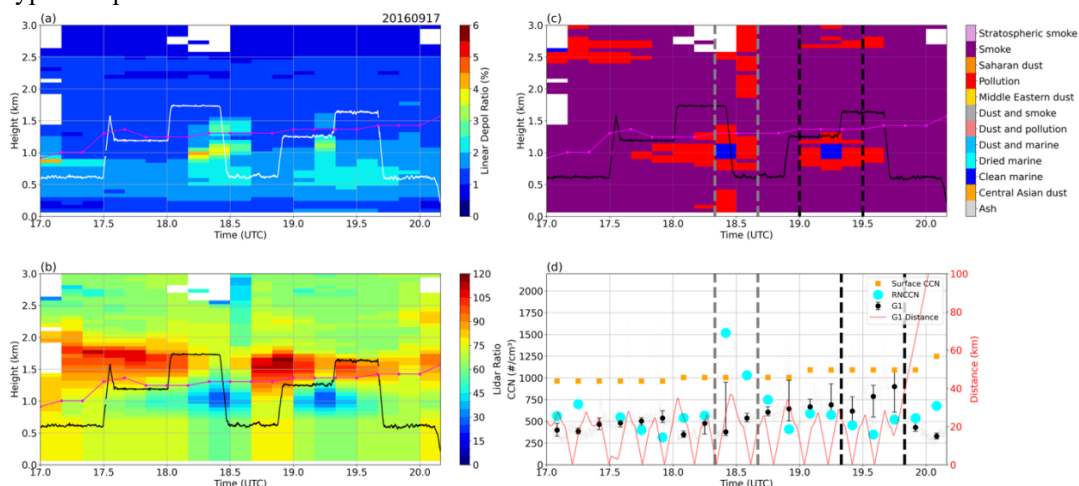


379 In contrast to the previous case, Figure 4 illustrates a more complex boundary layer  
 380 structure from September 17, 2016, characterized by pronounced vertical and temporal variability.  
 381 The time-height cross-sections (Figures 4a-c) reveal a multi-layered aerosol structure, with distinct  
 382 layers of high-LR “Pollution” and “Smoke” overlying a layer of low-LR “Clean marine” aerosol  
 383 around 1 km.

384 This increased complexity is reflected in the RNCCN performance. For samples when the  
 385 aircraft was within 30 km of the Raman lidar, the mean aircraft CCN concentration is  $560\text{ cm}^{-3}$ ,  
 386 while the corresponding RNCCN retrievals exhibit an RMSE of  $373\text{ cm}^{-3}$  and a positive bias of  
 387  $\sim 54\text{ cm}^{-3}$  relative to the aircraft (Table 1). These errors are larger than in Case #1.

388 Large discrepancies between RNCCN and in situ CCN tend to occur when aerosol  
 389 conditions are vertically and horizontally heterogeneous. For example, around 19:20–19:50 UTC,  
 390 the RNCCN–aircraft CCN difference increases after a period of strong vertical variability in  
 391 aerosol type (19:00–19:30 UTC; Figure 4c). The  $\sim 20$ -min offset can be explained by the lack of  
 392 exact collocation: the aircraft sampled within a 30-km radius rather than directly above the lidar,  
 393 so the aircraft and lidar likely sampled different air parcels that advected past the site at slightly  
 394 different times under heterogeneous conditions.

395 The most pronounced deviation occurs near 18:30 UTC. Two factors likely contribute: (a)  
 396 a vertical mismatch in aerosol type between the surface, the column sampled by the lidar, and the  
 397 aircraft level, such that the partial homogeneity assumption underlying the RNCCN retrieval is not  
 398 satisfied, and (b) a rapid change in aircraft altitude during 18:20–18:30 UTC, which increases the  
 399 variability of the time-averaged CCN estimate, as indicated by the large error bar on the G-1  
 400 measurements in this interval (Figure 4d). Overall, Case #2 demonstrates that RNCCN can still  
 401 capture the broad magnitude and variability of CCN under moderately heterogeneous conditions,  
 402 but retrieval errors increase when multiple aerosol types and sharp vertical transitions in aerosol  
 403 types are present.



404

405

Figure 4. Same as Figure 3, but for the case of September 17, 2016 (case #2).



#### 406 4.1.3 Case #3: Strongly Layered Aerosols

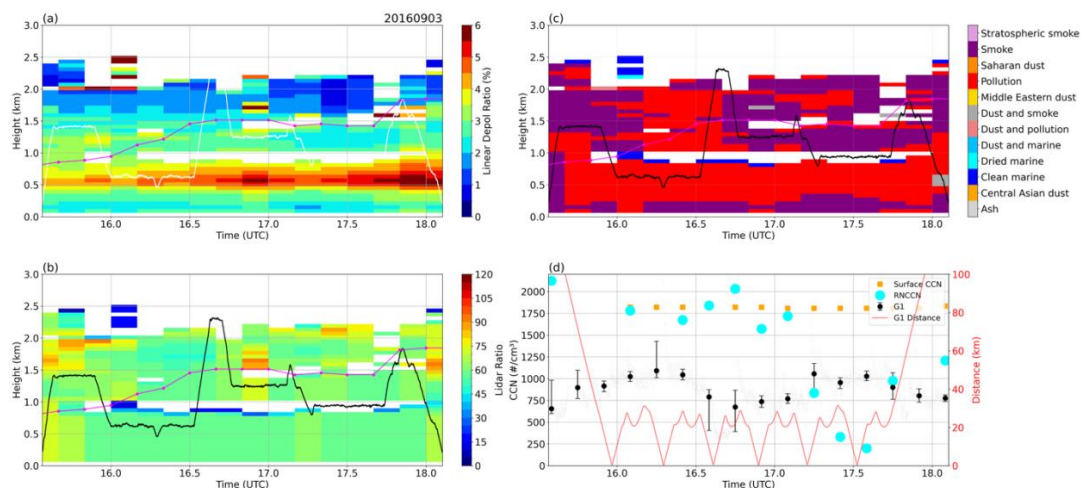
407 Figure 5 shows a case from 3 September 2016 (Case #3) that exhibits greater structural  
408 complexity than the previous cases. In Figures 5a-b, the LDR and LR fields reveal a strongly  
409 layered aerosol structure, and the aerosol-type classifications (Figure 5c) alternate between  
410 pollution, smoke, and occasional marine-like signatures. Grid cells without an assigned aerosol  
411 type at around 1 km in Figure 5c correspond directly to a “clean-air (no-detected-feature)” layer  
412 (Figure B-c), which indicates that no aerosol (or cloud/precipitation) feature is confidently detected  
413 and/or that aerosol extinction cannot be retrieved with sufficient quality in that layer (Thorsen et  
414 al., 2015).

415 The RNCCN algorithm relies on the ratio of dry extinction at height  $z$  to the surface value.  
416 This scaling requires valid, quality-controlled extinction retrievals at the reference level and at  
417 height  $z$  and a vertically continuous extinction profile between them. As a result, RNCCN is not  
418 reported within these clean-air (no-feature) layers. Where RNCCN is reported above the gap, its  
419 interpretation may be uncertain because the extinction scaling is effectively applied across a layer  
420 with missing or low-quality extinction, so the connection between the surface aerosol and the  
421 elevated layer may not be confidently established.

422 The comparison with in situ CCN measurements (Figure 5d) reflects this case’s complexity.  
423 Overall, RNCCN performance is much worse than in the first two cases. For samples collected  
424 within 30 km of the Raman lidar, the mean aircraft CCN concentration is  $899 \text{ cm}^{-3}$ , whereas  
425 RNCCN exhibits an RMSE of  $1276 \text{ cm}^{-3}$  and a substantial positive bias of  $701 \text{ cm}^{-3}$  (Table 1).  
426 These large discrepancies indicate that the retrieval substantially overestimates CCN under these  
427 heterogeneous, multi-layered aerosol type conditions.

428 The degraded performance coincides with (1) vertically intermittent clean-air (no-feature)  
429 regions that break the column into poorly constrained segments and (2) pronounced aerosol-type  
430 variability with height. Unlike Case #1, where the aerosol column was relatively uniform and well  
431 classified, this example highlights conditions in which the RNCCN assumption of a vertically  
432 homogeneous, well-characterized sub-cloud aerosol layer is clearly not held, leading to larger  
433 retrieval uncertainties.

434



435

436 Figure 5. Same as Figure 3, but for the case of September 3, 2016 (case #3).

437 **4.2 Statistical Evaluation of RNCCN**

438 While the case studies in Section 4.1 provide a detailed, qualitative view of RNCCN  
 439 performance under specific conditions, they do not indicate how representative those behaviors  
 440 are across the full HI-SCALE dataset/cases. A statistical analysis is necessary to (i) generalize the  
 441 case-study findings to all available flights and (ii) relate RNCCN deviation from aircraft  
 442 measurements to a more objective measure of aerosol complexity.

443 To examine how aerosol variability influences RNCCN performance, all G-1–RNCCN  
 444 comparisons were aggregated into 10-minute windows. Each window requires (i) at least one valid  
 445 G-1 CCN measurement and one valid RNCCN estimate, and (ii) a mean aircraft–Raman lidar  
 446 distance separation < 30 km. Flight days with fewer than three valid windows are excluded from  
 447 the case-level analysis.

448 To quantify the complexity of the aerosol column for each case, we use the kNN aerosol-  
 449 type classifications derived from Raman lidar measurements (LDR and LR). For every valid 10-  
 450 minute window that meets the collocation criteria described above, and for all RNCCN vertical  
 451 levels between the surface and the maximum aircraft altitude, we count occurrences of each aerosol  
 452 type and the clean-air (no-detected-feature) category, which represents layers where aerosol  
 453 extinction is not retrievable and can interrupt the extinction scaling used by RNCCN. Counts are  
 454 summed over all valid windows for a given case and converted to fractional occurrences  $p_i$ . A  
 455 simple heterogeneity index is then defined using the Gini impurity (Breiman et al., 1984):

456 
$$H = 1 - \sum_i p_i^2, \quad (2)$$

457 such that H closes to 0 corresponds to a nearly uniform aerosol column dominated by a single type,  
 458 while larger values reflect increased mixing among multiple aerosol types and/or substantial no-  
 459 feature (extinction-retrieval gap) layers below the aircraft.

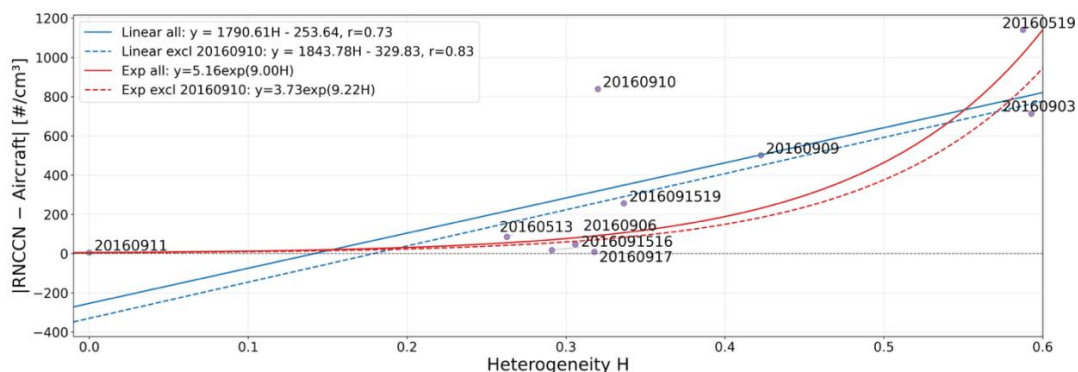


460 For each case, we compute the mean G-1 CCN and RNCCN CCN across all valid windows  
 461 and use  $|RNCCN-G1|$  as a case-level measure of retrieval error. Figure 6 summarizes the  
 462 relationship between vertical heterogeneity below aircraft flight altitude and RNCCN  
 463 performance. Each point represents a flight day, labeled by its case ID. The 20160911 case ( $H \approx 0$ )  
 464 exhibits a vertically uniform aerosol environment with minimal type transitions and no missing  
 465 layers and correspondingly shows the smallest RNCCN–G-1 difference, which is consistent with  
 466 the homogeneous structure documented in Figure 3. Larger discrepancies occur for cases with  
 467 elevated heterogeneity (e.g.,  $H > 0.5$ ).

468 Overall, Figure 6 shows a modest positive association between RNCCN–G-1 discrepancies  
 469 and heterogeneity index, although substantial scatter remains at intermediate  $H$ . A linear fit  
 470 indicates moderate correlations (0.73 or 0.83 when excluding 10 September 2016), consistent with  
 471 an overall increase in discrepancy with  $H$ . This conclusion/trend holds when the error is expressed  
 472 as either an absolute difference or a relative difference normalized by the mean G-1 CCN. This  
 473 result supports the interpretation that the extinction-scaling approach used in RNCCN is more  
 474 likely to produce large errors in vertically complex/heterogeneous conditions (larger  $H$  values),  
 475 not just in the specific examples shown in Figures 3–5.

476 At the same time, we emphasize that  $H$  summarizes heterogeneity in LR/LDR-derived  
 477 aerosol typing and should therefore be interpreted as an indicator of vertical-complexity rather  
 478 than a complete predictor of RNCCN error. RNCCN discrepancies can also be driven by strong  
 479 vertical extinction gradients and/or retrieval and representativeness uncertainties that are not fully  
 480 captured by  $H$ ; the 10 September 2016 outlier is discussed in Appendix C.

481



482

483 Figure 6. Case-level relationship between aerosol heterogeneity  $H$  and RNCCN Aircraft difference  
 484  $|RNCCN-Aircraft|$ . Each point shows one flight day, labeled by its case ID. Labels of the form  
 485 YYYYMMDDHH (e.g., 2016091516 and 2016091519) indicate the date and central UTC hour of  
 486 the flight segment. Solid lines represent linear and exponential fits using all cases, while dashed  
 487 lines exclude the 20160910-outlier case.

488 **5. Summary and Conclusions**



489           The objective of this study is to assess how vertical variability in aerosol optical properties  
490 (used as a proxy for aerosol type/compositional variability) affects the performance of CCN  
491 profiles provided by the RNCCN. This assessment was carried out using in situ aircraft CCN  
492 measurements from the HI-SCALE field study conducted near the ARM SGP site.

493           The RNCCN retrieval method relies on scaling surface CCN measurements with vertically  
494 resolved aerosol extinction profiles from Raman lidar and assumes a vertically uniform aerosol  
495 composition. However, this assumption may not always be valid, and therefore, this study  
496 specifically investigated whether the vertical variability in lidar-inferred aerosol classes (based on  
497 lidar ratio and linear depolarization ratio) can serve as an indicator of reduced RNCCN retrieval  
498 confidence. We hypothesize that violations of this vertical uniformity assumption, i.e., strong  
499 vertical heterogeneity in these lidar-inferred classes, will degrade RNCCN performance. To test  
500 this hypothesis, we developed a kNN-based classification framework using data from the DeLiAn  
501 database. This framework was used to generate the vertical distributions of aerosol classes. Under  
502 different boundary layer vertical aerosol structures, we then compared RNCCN with in situ CCN  
503 concentrations from the G-1 aircraft.

504           The results show that RNCCN performance degrades as vertical aerosol complexity  
505 increases. For vertically homogeneous, pollution-dominated columns, RNCCN closely matches  
506 aircraft CCN, indicating that extinction scaling works well when aerosol composition is nearly  
507 uniform. As embedded layers of differing aerosol classes/types and moderate vertical structure  
508 appear, RNCCN errors grow. In strongly layered scenes with alternating aerosol classes/types,  
509 intermittent no-feature regions, or gaps that disconnect elevated aerosol from the surface layer, the  
510 difference between RNCCN and aircraft-measured CCN is large.

511           To generalize beyond individual examples, we introduced a heterogeneity index based on  
512 the vertical distribution of kNN-derived aerosol classes/types. Statistics show a tendency for  
513 RNCCN retrieval error to increase with this heterogeneity metric ( $H$ ), quantitatively confirming  
514 that aerosol complexity is one of the key controls on RNCCN reliability, even though RNCCN  
515 discrepancies can also be driven by strong vertical extinction gradients and/or retrieval and  
516 representativeness uncertainties that are not fully captured by  $H$ .

517           This methodology can be used to enhance RNCCN, either within the existing product or  
518 as a companion dataset, by providing kNN-derived aerosol-class/type (optical regime) profiles and  
519 a heterogeneity index ( $H$ ) together with simple quality flags that classify columns as relatively  
520 homogeneous or heterogeneous. These additions offer a practical indicator of RNCCN confidence  
521 and enable objective filtering or stratification of RNCCN profiles in subsequent analyses. In  
522 practice,  $H$  can be computed for each RNCCN profile using a temporal window (e.g., 30–60 min)  
523 and over a specified lower-tropospheric layer (e.g., 0–3 km). A categorical quality flag can also be  
524 assigned from  $H$  to distinguish higher-confidence homogeneous cases from lower-confidence  
525 heterogeneous cases.

526           The proposed ML-based assessment framework improves our ability to interpret RNCCN  
527 accuracy and to identify conditions under which extinction-scaling approaches are relatively  
528 trustworthy. This supports more robust use of long-term CCN vertical distributions for model



529 evaluation and for studying aerosol–cloud interactions. The framework is not limited to the current  
530 RNCCN implementation and can be extended to other CCN-profile retrievals from Raman or high-  
531 spectral-resolution lidars, provided that both LR and LDR are available. Future work could refine  
532 the classification scheme by incorporating additional, independent lidar observables (e.g.,  
533 multiwavelength backscatter or depolarization), thereby improving aerosol classification based on  
534 optical properties and RNCCN assessment in more complex aerosol environments.

#### 535 **Data availability**

536 Data for this article can be downloaded at: <https://adc.arm.gov/discovery/>. Retrieved profiles of  
537 cloud condensation nuclei (CCN) number concentration from the RNCCNPROF1KULKARNI  
538 value-added product (VAP) are available at the Atmospheric Radiation Measurement (ARM) Data  
539 Center via <https://doi.org/10.5439/1813858> (ARM, 2023). Additionally, cloud condensation nuclei  
540 (CCN) measurements from the HI-SCALE (Holistic Interactions of Shallow Clouds, Aerosols, and  
541 Land-Ecosystems) field campaign can be accessed at [https://iop.arm.gov/2016/sgp/hiscale/mei-  
542 ccn/](https://iop.arm.gov/2016/sgp/hiscale/mei-ccn/). The DeliAn data are available at <https://doi.org/10.5281/zenodo.7751752> (Floutsi et al.,  
543 2023).

#### 544 **Author contributions**

545 Writing (original draft preparation): JT; Visualization: JT; Editing: JT, GK, JC, JS, DZ, PW, FM;  
546 Methodology: JT, GK, JC, JS, DZ, PW, FM; Data curation: JT, GK; Supervision: JC, JS

#### 547 **Competing interests**

548 The authors declare no competing interests.

#### 549 **Acknowledgments**

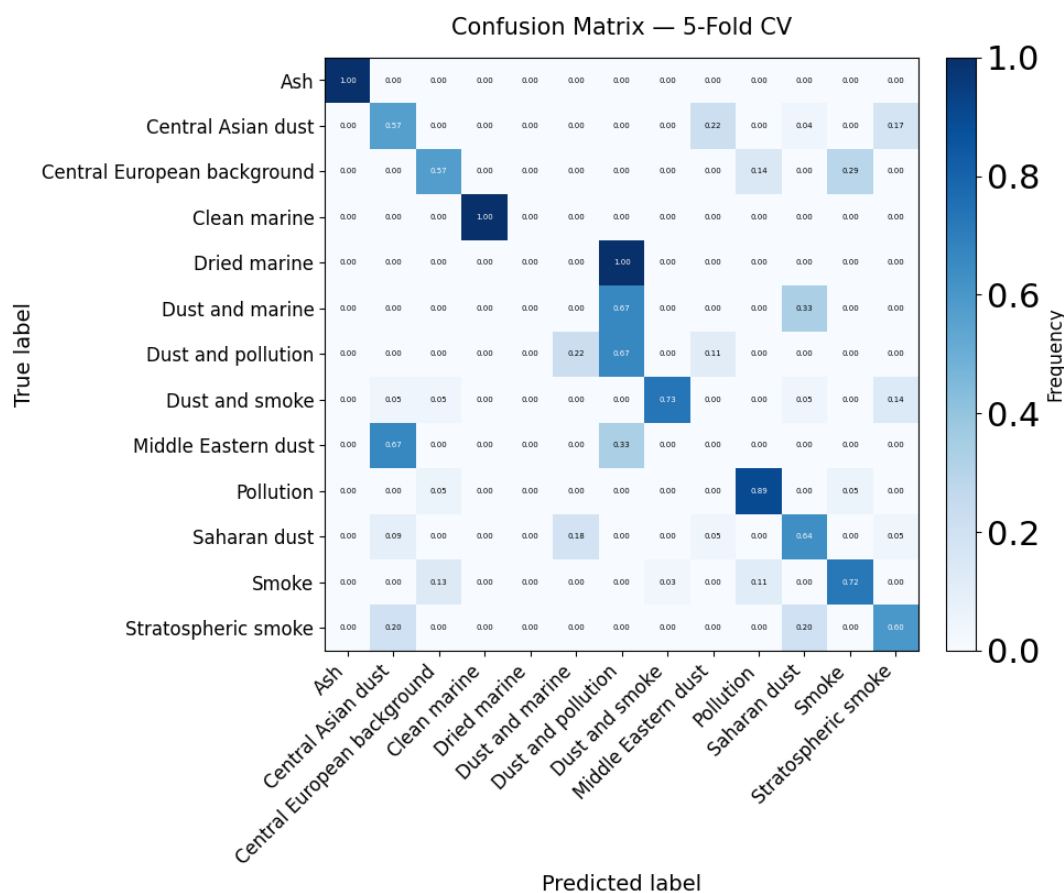
550 This research is supported by, and data were obtained from, the ARM user facility, a U.S.  
551 Department of Energy (DOE) Office of Science user facility managed by the Biological and  
552 Environmental Research (BER) program. Pacific Northwest National Laboratory is operated by  
553 Battelle for the U.S. Department of Energy under Contract DE-AC05-76RLO1830. Gourihar  
554 Kulkarni was supported by the Atmospheric System Research (ASR) program as part of the U.S.  
555 Department of Energy (DOE) Office of Science's Biological and Environmental Research (BER)  
556 program under the Pacific Northwest National Laboratory (PNNL) project:57131.

#### 557 **Appendix A**

558 Classification performance is type-dependent. The model demonstrates high fidelity in  
559 distinguishing optically unique aerosol types (“Ash”, “Smoke”, “Pollution”, and “Clean Marine”).  
560 For example, “Ash” and “Clean marine” are identified with near-perfect accuracy. The classifier  
561 also effectively resolves key anthropogenic types like Pollution (89% accuracy) and Smoke (72%  
562 accuracy). Conversely, and as expected, classification ambiguity increases for aerosol classes with  
563 overlapping optical properties. This is most evident among different dust types and mixtures. For  
564 instance, the model struggles to differentiate regional dusts: 67% of “Middle Eastern dust” is



565 misclassified as “Central Asian dust”. Similarly, mixed-phase classes are challenging. While “Dust and pollution” is correctly identified 67% of the time, the remaining 22% (11%) is misclassified  
 566 as “Dust and marine” (“Middle Eastern dust”), indicating confusion between a mixture and one of  
 567 its potential pure components. These patterns do not indicate a model failure, and they are  
 568 consistent with the expected difficulty of distinguishing internally mixed or regionally similar dust  
 569 types using only LDR and LR.  
 570  
 571



572

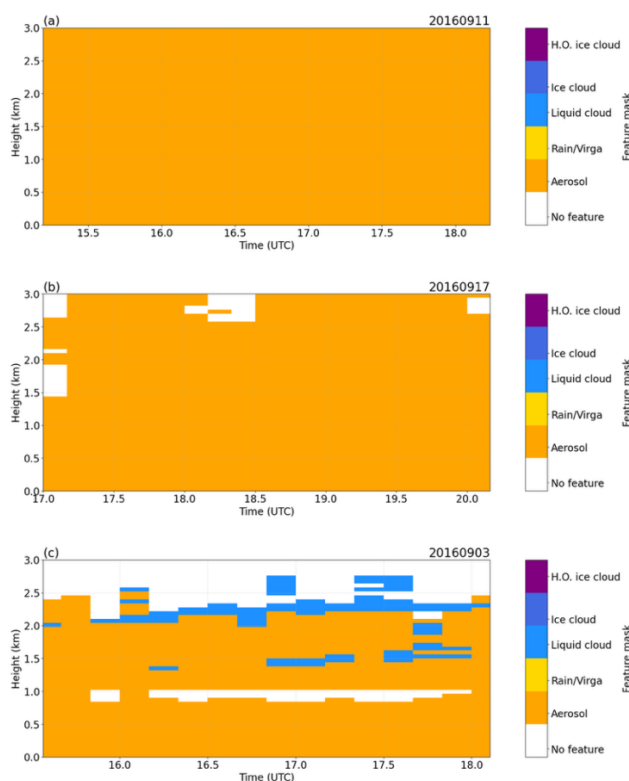
573 Figure A. Row-normalized confusion matrix from 5-fold stratified cross-validation. Each row  
 574 represents the true aerosol class, and each column shows the predicted class. Values on the diagonal  
 575 represent the accuracy for each class, while off-diagonal values indicate misclassifications.

576 **Appendix B**

577 The feature masks shown in Figure B are derived from the Raman Lidar Profiles, Feature Detection  
 578 and Extinction (RLPROF-FEX) Value-Added Product (VAP) (Chand et al., 2019). The RLPROF-



579 FEX algorithm identifies and classifies atmospheric targets, including aerosol layers, liquid clouds,  
 580 ice clouds, and precipitation, using automated feature detection methods described in Thorsen et  
 581 al. (2015) and Thorsen and Fu (2015).



582

583 Figure B. Feature mask from Raman Lidar on (a) September 11, 2016 (case #1), (b) September 17,  
 584 2016 (case #2), and (c) September 3, 2016 (case #3).

### 585 Appendix C

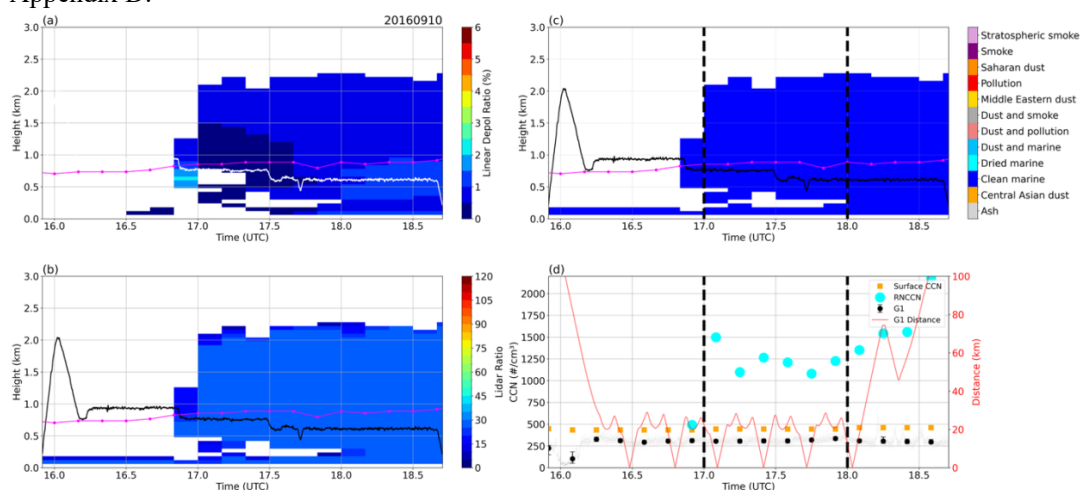
586 In Figure. C1-d (case 10 September 2016), RNCCN substantially overestimates the aircraft  
 587 CCN. This bias is not accompanied by a great change in LR or LDR with height, and the kNN  
 588 classifier assigns the same aerosol type at the surface and flight level, probably suggesting that the  
 589 error is not driven by a major aerosol-type transition in LR–LDR space. Instead, the Raman-lidar  
 590 dry-corrected extinction increases sharply with height during this period (Figure B2), yielding an  
 591 unusually large dry-extinction ratio relative to the near-surface reference level. Because RNCCN  
 592 scales surface CCN by this ratio, the enhanced extinction gradient directly amplifies the retrieved  
 593 CCN aloft and explains the overestimate mechanistically.

594 The origin of this extreme extinction gradient cannot be uniquely determined here. One  
 595 possibility is physical: an elevated aerosol layer with substantially higher aerosol loading and/or  
 596 different microphysical characteristics than near the surface, even though LR and LDR remain



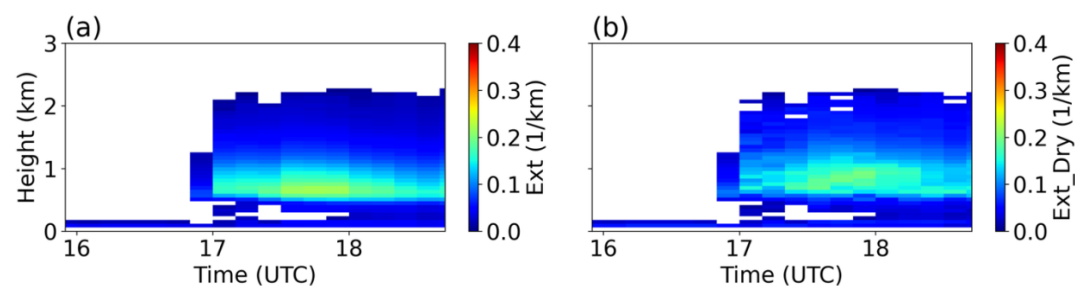
597 within the same kNN aerosol-type class (i.e., similar LR–LDR does not imply vertically uniform  
 598 loading or a constant extinction-to-CCN relationship). Alternatively, the gradient may be  
 599 influenced by retrieval and representativeness effects, for example, low-SNR/QC limitations  
 600 (including the intervening no-feature interval), and/or imperfect spatial–temporal matching  
 601 between the aircraft and the surface–lidar column despite the less than 30 km distance.

602 Additional note for Figure C1-c, at SGP, the kNN ‘marine’ label likely represents a  
 603 clean/background regime rather than true sea-salt influence. Supporting analysis is given in  
 604 Appendix D.



605

606 Figure C1. Same as Figure 3, but for the case of September 10, 2016.



607

608 Figure C2. Time–height cross sections of Raman-lidar aerosol extinction for Case (10 September  
 609 2016). (a) Lidar extinction coefficient ( $Ext$ ,  $km^{-1}$ ). (b) Dry-corrected aerosol extinction coefficient  
 610 ( $Ext_{Dry}$ ,  $km^{-1}$ ) directly used in the RNCCN.

### 611 Appendix D

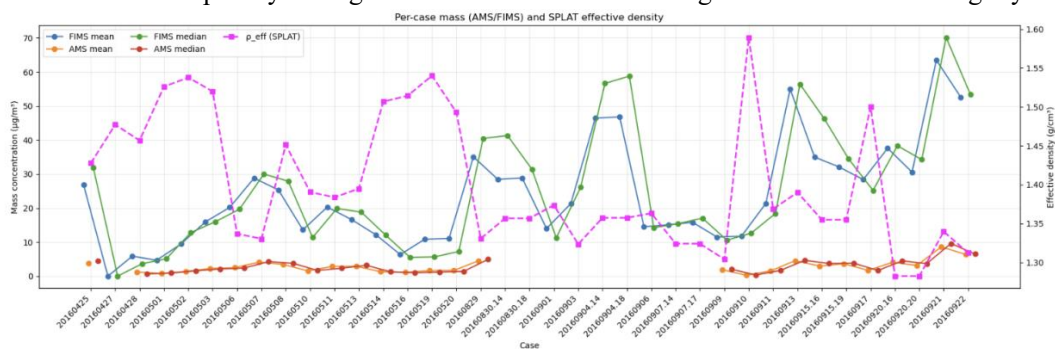
612 This subsection evaluates the physical meaning of the kNN-derived ‘marine’ aerosol class  
 613 at SGP and clarifies how this label should be interpreted when assessing RNCCN performance at  
 614 SGP. Because the SGP site is far from any oceanic influence, a truly sea-salt–dominated aerosol  
 615 could be unlikely. To investigate whether this classification is physically plausible, we compared



616 independent aircraft measurements from the Aerosol Mass Spectrometer (AMS), Fluorescent  
 617 Aerosol-Size Time-of-Flight Mobility Spectrometer (FIMS), and SPLAT (Single Particle Laser  
 618 Ablation Time-of-Flight Mass Spectrometer).

619 For each flight day, AMS provided non-refractory submicron mass (sulfate, nitrate,  
 620 ammonium, chloride, organics), while FIMS measured the full aerosol size distribution, which  
 621 includes AMS-detectable species plus coarse-mode dust and any potential sea-salt (Fast et al.,  
 622 2022). To estimate aerosol mass from FIMS, we used composition-dependent effective densities  
 623 derived from SPLAT, which reports per-case fractional contributions of major aerosol classes.  
 624 Combining the FIMS size distribution with SPLAT-derived effective density allowed us to infer a  
 625 bulk mass concentration that should exceed AMS if marine or dust aerosols were abundant.

626 However, for 10 September 2016, the FIMS-inferred mass was not significantly larger than  
 627 AMS, and both instruments showed relatively low aerosol loading compared to other flight days  
 628 (Figure D). This may indicate that this case was not dominated by sea salt or dust. Instead, the  
 629 scene appears to represent a clean, low aerosol airmass. Under such conditions of extremely weak  
 630 aerosol signal, the LDR–LR features that drive the kNN classification become less distinctive, and  
 631 the algorithm can misclassify “clean” conditions as “marine” because both exhibit weak  
 632 depolarization and moderate lidar ratios. Thus, we suspect that the “marine” label on 2016-09-10  
 633 does not imply the presence of sea salt but is better interpreted as a clean background regime with  
 634 very low continental aerosol influence. This interpretation is consistent with ARM’s use of the  
 635 term “clean marine” in remote regions (e.g., Kennaook–Cape Grim), where it denotes an airmass  
 636 with minimal anthropogenic or continental contributions, not necessarily one dominated by  
 637 oceanic sea-salt particles. Our results, therefore, suggest that the marine classification at SGP may  
 638 reflect the absence of pollution, rather than true marine aerosol, and that future versions of the  
 639 classifier should explicitly distinguish “clean” from “marine” regimes to avoid this ambiguity.



640

641 Figure D. Per-case aerosol mass derived from the Fast Integrated Mobility Spectrometer (FIMS)  
 642 and the Aerosol Mass Spectrometer (AMS), together with Single Particle Lagrangian Integrated  
 643 Trajectory (SPLAT)–derived effective particle density ( $\rho_{\text{eff}}$ ). FIMS aerosol mass (mean and  
 644 median) is estimated from measured aerosol size distributions using the case-specific effective  
 645 density ( $\rho_{\text{eff}}$ ), while AMS mass represents non-refractory submicron aerosol species, including  
 646 sulfate ( $\text{SO}_4^{2-}$ ), nitrate ( $\text{NO}_3^-$ ), ammonium ( $\text{NH}_4^+$ ), chloride ( $\text{Cl}^-$ ), and organic aerosol (Org).



647 **References**

- 648 Atmospheric Radiation Measurement (ARM) user facility: Retrieved number concentration of  
649 CCN profile from Kulkarni first algorithm (RNCCNPROF1KULKARNI), Southern Great  
650 Plains (C1), 25 Jan 2016–18 Oct 2023, *ARM Data Center*,  
651 <https://doi.org/10.5439/1813858>, 2023.
- 652 Bellet, V., Fauvel, M., and Inglada, J.: Land cover classification with Gaussian processes using  
653 spatio-spectro-temporal features, *IEEE Trans. Geosci. Remote Sens.*, **61**, 1–21,  
654 <https://doi.org/10.1109/TGRS.2023.3234527>, 2023.
- 655 Bellouin, N., Quaas, J., Gryspeerdt, E., Kinne, S., Stier, P., Watson-Parris, D., Boucher, O.,  
656 Carslaw, K. S., Christensen, M., Daniau, A. L., Dufresne, J. L., Feingold, G., Fiedler, S.,  
657 Forster, P., Gettelman, A., Haywood, J. M., Lohmann, U., Malavelle, F., Mauritsen, T.,  
658 McCoy, D. T., Myhre, G., Mülmenstädt, J., Neubauer, D., Possner, A., Rugenstein, M., Sato,  
659 Y., Schulz, M., Schwartz, S. E., Sourdeval, O., Storelvmo, T., Toll, V., Winker, D., and  
660 Stevens, B.: Bounding Global Aerosol Radiative Forcing of Climate Change, *Reviews of*  
661 *Geophysics*, **58**, 10.1029/2019rg000660, 2020.
- 662 Breiman, L., Friedman, J. H., Olshen, R. A., and Stone, C. J.: *Classification and regression trees*,  
663 Wadsworth International Group, Belmont, CA, USA, 1984.
- 664 Bohlmann, S., Baars, H., Radenz, M., Engelmann, R., and Macke, A.: Ship-borne aerosol profiling  
665 with lidar over the Atlantic Ocean: from pure marine conditions to complex dust–smoke  
666 mixtures, *Atmospheric Chemistry and Physics*, **18**, 9661–9679, 10.5194/acp-18-9661-  
667 2018, 2018.
- 668 Brendecke, J., Dong, X., Xi, B., and Zheng, X.: Maritime Aerosol and CCN Profiles Derived From  
669 Ship-Based Measurements Over Eastern North Pacific During MAGIC, *Earth and Space*  
670 *Science*, **9**, 10.1029/2022ea002319, 2022.
- 671 Burton, S. P., Ferrare, R. A., Hostetler, C. A., Hair, J. W., Rogers, R. R., Obland, M. D., Butler, C.  
672 F., Cook, A. L., Harper, D. B., and Froyd, K. D.: Aerosol classification using airborne High  
673 Spectral Resolution Lidar measurements – methodology and examples, *Atmospheric*  
674 *Measurement Techniques*, **5**, 73–98, 10.5194/amt-5-73-2012, 2012.
- 675 Camps-Valls, G. and Bruzzone, L. (Eds.): *Kernel methods for remote sensing data analysis*, 420  
676 pp., John Wiley & Sons, Ltd., Chichester, UK, <https://doi.org/10.1002/9780470748992>,  
677 2009.
- 678 Chand, D., Newsom, R., Thorsen, T., Cromwell, E., Sivaraman, C., Flynn, C., Shilling, J., and  
679 Comstock, J.: Aerosol and Cloud Optical Properties from the ARM Raman Lidars: The  
680 Feature Detection and Extinction (FEX) Value-Added Product,  
681 DOI:<https://doi.org/10.2172/1560857>, 2019.
- 682 Choudhury, G. and Tesche, M.: Assessment of CALIOP-Derived CCN Concentrations by In Situ  
683 Surface Measurements, *Remote Sensing*, **14**, 3342, 10.3390/rs14143342, 2022a.
- 684 Choudhury, G. and Tesche, M.: Estimating cloud condensation nuclei concentrations from  
685 CALIPSO lidar measurements, *Atmospheric Measurement Techniques*, **15**, 639–654,  
686 10.5194/amt-15-639-2022, 2022b.
- 687 Clarke, A. D., Uehara, T., and Porter, J. N.: Atmospheric nuclei and related aerosol fields over the  
688 Atlantic: clean subsiding air and continental pollution during ASTEX, *J. Geophys. Res.-*  
689 *Atmos.*, **102**, 25281–25292, 1997.
- 690 Dawson, W., K., Ferrare, A., R., Moore, H., R., Clayton, B., M., Thorsen, J., T., and Eloranta, W.,  
691 E.: Ambient Aerosol Hygroscopic Growth From Combined Raman Lidar and HSRL,



- 692 Journal of Geophysical Research: Atmospheres, 125, e2019JD031708,  
693 10.1029/2019jd031708, 2020.
- 694 Dong, X., Schwantes, A. C., Xi, B., and Wu, P.: Investigation of the marine boundary layer cloud  
695 and CCN properties under coupled and decoupled conditions over the Azores, Journal of  
696 Geophysical Research: Atmospheres, 120, 6179-6191, 10.1002/2014jd022939, 2015.
- 697 Engelmann, R., Kanitz, T., Baars, H., Heese, B., Althausen, D., Skupin, A., Wandinger, U.,  
698 Komppula, M., Stachlewska, I. S., Amiridis, V., Marinou, E., Mattis, I., Linné, H., and  
699 Ansmann, A.: The automated multiwavelength Raman polarization and water-vapor lidar  
700 Polly<sup>XT</sup>: the neXT generation, Atmospheric Measurement Techniques, 9,  
701 1767-1784, 10.5194/amt-9-1767-2016, 2016.
- 702 Engelmann, R., Ansmann, A., Ohneiser, K., Griesche, H., Radenz, M., Hofer, J., Althausen, D.,  
703 Dahlke, S., Maturilli, M., Veselovskii, I., Jimenez, C., Wiesen, R., Baars, H., Bühl, J.,  
704 Gebauer, H., Haarig, M., Seifert, P., Wandinger, U., and Macke, A.: Wildfire smoke, Arctic  
705 haze, and aerosol effects on mixed-phase and cirrus clouds over the North Pole region  
706 during MOSAiC: an introduction, Atmospheric Chemistry and Physics, 21, 13397-13423,  
707 10.5194/acp-21-13397-2021, 2021.
- 708 Fast, J. D., Bell, D. M., Kulkarni, G., Liu, J., Mei, F., Saliba, G., Shilling, J. E., Suski, K.,  
709 Tomlinson, J., Wang, J., Zaveri, R., and Zelenyuk, A.: Using aircraft measurements to  
710 characterize subgrid-scale variability of aerosol properties near the Atmospheric Radiation  
711 Measurement Southern Great Plains site, Atmospheric Chemistry and Physics, 22, 11217-  
712 11238, 10.5194/acp-22-11217-2022, 2022.
- 713 Fast, J. D., Berg, L. K., Alexander, L., Bell, D., D'Ambro, E., Hubbe, J., Kuang, C., Liu, J., Long,  
714 C., Matthews, A., Mei, F., Newsom, R., Pekour, M., Pinterich, T., Schmid, B.,  
715 Schobesberger, S., Shilling, J., Smith, J. N., Springston, S., Suski, K., Thornton, J. A.,  
716 Tomlinson, J., Wang, J., Xiao, H., and Zelenyuk, A.: Overview of the hi-scale field  
717 campaign a new perspective on shallow convective clouds, 10.1175/BAMS-D-18-0030.1,  
718 2019.
- 719 Ferrare, R., Hair, J., Hostetler, C., Shingler, T., Burton, S. P., Fenn, M., Clayton, M., Scarino, A.  
720 J., Harper, D., Seaman, S., Cook, A., Crosbie, E., Winstead, E., Ziemba, L., Thornhill, L.,  
721 Robinson, C., Moore, R., Vaughan, M., Sorooshian, A., Schlosser, J. S., Liu, H., Zhang, B.,  
722 Diskin, G., Digangi, J., Nowak, J., Choi, Y., Zuidema, P., and Chellappan, S.: Airborne  
723 HSRL-2 measurements of elevated aerosol depolarization associated with non-spherical  
724 sea salt, Frontiers in Remote Sensing, 4, 10.3389/frsen.2023.1143944, 2023.
- 725 Floutsi, A. A., Baars, H., Engelmann, R., Althausen, D., Ansmann, A., Bohlmann, S., Heese, B.,  
726 Hofer, J., Kanitz, T., Haarig, M., Ohneiser, K., Radenz, M., Seifert, P., Skupin, A., Yin, Z.,  
727 Abdullaev, S. F., Komppula, M., Filioglou, M., Giannakaki, E., Stachlewska, I. S., Janicka,  
728 L., Bortoli, D., Marinou, E., Amiridis, V., Gialitaki, A., Mamouri, R.-E., Barja, B., and  
729 Wandinger, U.: DeLiAn – a growing collection of depolarization ratio, lidar ratio and  
730 Ångström exponent for different aerosol types and mixtures from ground-based lidar  
731 observations, Atmospheric Measurement Techniques, 16, 2353-2379, 10.5194/amt-16-  
732 2353-2023, 2023.
- 733 Ghan, S. J., Liu, X., Easter, R. C., Zaveri, R., Rasch, P. J., Yoon, J.-H., and Eaton, B.: Toward a  
734 Minimal Representation of Aerosols in Climate Models: Comparative Decomposition of  
735 Aerosol Direct, Semidirect, and Indirect Radiative Forcing, Journal of Climate, 25, 6461-  
736 6476, 10.1175/jcli-d-11-00650.1, 2012.



- 737 Ghan, S. J. and Collins, D. R.: Use of in situ data to test a Raman lidar-based cloud condensation  
738 nuclei remote sensing method, *J. Atmos. Oceanic Technol.*, **21**, 387–394,  
739 [https://doi.org/10.1175/1520-0426\(2004\)021<0387:UOISDT>2.0.CO;2](https://doi.org/10.1175/1520-0426(2004)021<0387:UOISDT>2.0.CO;2), 2004.
- 740 Ghan, S. J., Rissman, T. A., Elleman, R., Ferrare, R. A., Turner, D., Flynn, C., Wang, J., Ogren, J.,  
741 Hudson, J., Jonsson, H. H., Vanreken, T., Flagan, R. C., and Seinfeld, J. H.: Use of in situ  
742 cloud condensation nuclei, extinction, and aerosol size distribution measurements to test a  
743 method for retrieving cloud condensation nuclei profiles from surface measurements,  
744 *Journal of Geophysical Research*, **111**, 10.1029/2004jd005752, 2006.
- 745 Groß, S., Freudenthaler, V., Wirth, M., and Weinzierl, B.: Towards an aerosol classification scheme  
746 for future <scp>EarthCARE</scp> lidar observations and implications for research needs,  
747 *Atmospheric Science Letters*, **16**, 77–82, 10.1002/asl2.524, 2015.
- 748 Groß, S., Freudenthaler, V., Haarig, M., Ansmann, A., Toledano, C., Mateos, D., Seibert, P.,  
749 Mamouri, R.-E., Nisantzi, A., Gasteiger, J., Dollner, M., Tipka, A., Schöberl, M., Teri, M.,  
750 and Weinzierl, B.: Characterization of aerosol over the eastern Mediterranean by  
751 polarization-sensitive Raman lidar measurements during A-LIFE – aerosol type  
752 classification and type separation, *Atmospheric Chemistry and Physics*, **25**, 3191–3211,  
753 10.5194/acp-25-3191-2025, 2025.
- 754 Gryspeerd, E., Povey, A. C., Grainger, R. G., Hasekamp, O., Hsu, N. C., Mulcahy, J. P., Sayer, A.  
755 M., and Sorooshian, A.: Uncertainty in aerosol–cloud radiative forcing is driven by clean  
756 conditions, *Atmospheric Chemistry and Physics*, **23**, 4115–4122, 10.5194/acp-23-4115-  
757 2023, 2023.
- 758 Haarig, M., Ansmann, A., Gasteiger, J., Kandler, K., Althausen, D., Baars, H., Radenz, M., and  
759 Farrell, D. A.: Dry versus wet marine particle optical properties: RH dependence of  
760 depolarization ratio, backscatter, and extinction from multiwavelength lidar measurements  
761 during SALTRACE, *Atmospheric Chemistry and Physics*, **17**, 14199–14217, 10.5194/acp-  
762 17-14199-2017, 2017.
- 763 Kanitz, T., Ansmann, A., Engelmann, R., and Althausen, D.: North-south cross sections of the  
764 vertical aerosol distribution over the Atlantic Ocean from multiwavelength  
765 Raman/polarization lidar during Polarstern cruises, *Journal of Geophysical Research:  
766 Atmospheres*, **118**, 2643–2655, 10.1002/jgrd.50273, 2013.
- 767 Kapustin, V. N., Clarke, A. D., Shinozuka, Y., Howell, S., Brekhovskikh, V., Nakajima, T., and  
768 Higurashi, A.: On the determination of a cloud condensation nuclei from satellite:  
769 Challenges and possibilities, *Journal of Geophysical Research: Atmospheres*, **111**,  
770 10.1029/2004jd005527, 2006.
- 771 Kim, M.-H., Omar, A. H., Tackett, J. L., Vaughan, M. A., Winker, D. M., Trepte, C. R., Hu, Y., Liu,  
772 Z., Poole, L. R., Pitts, M. C., Kar, J., and Magill, B. E.: The CALIPSO version 4 automated  
773 aerosol classification and lidar ratio selection algorithm, *Atmospheric Measurement  
774 Techniques*, **11**, 6107–6135, 10.5194/amt-11-6107-2018, 2018.
- 775 Kulkarni, G., Mei, F., Sivaraman, C., Wang, J., Shilling, J. E., Newsom, R. K., Christensen, M. W.,  
776 Berg, L. K., and Fast, J. D.: Assessment of Extinction-, Satellite-, and Model-Based Vertical  
777 Cloud Condensation Nuclei (CCN) Retrieval Methods Using Airborne CCN  
778 Measurements Over the Southern Great Plains, *Journal of Geophysical Research:  
779 Atmospheres*, **130**, 10.1029/2024jd042565, 2025.
- 780 Kulkarni, G., Sivaraman, C., and Shilling, J. E.: Retrieved number concentration of cloud  
781 condensation nuclei (RNCCN) profile value-added product report, DOE/SC-ARM-TR-  
782 292, <https://doi.org/10.2172/2205615>, 2023.



- 783 Lenhardt, E. D., Gao, L., Redemann, J., Xu, F., Burton, S. P., Cairns, B., Chang, I., Ferrare, R. A.,  
784 Hostetler, C. A., Saide, P. E., Howes, C., Shinozuka, Y., Stamnes, S., Kacarab, M.,  
785 Dobracki, A., Wong, J., Freitag, S., and Nenes, A.: Use of lidar aerosol extinction and  
786 backscatter coefficients to estimate cloud condensation nuclei (CCN) concentrations in  
787 the southeast Atlantic, *Atmospheric Measurement Techniques*, 16, 2037-2054,  
788 10.5194/amt-16-2037-2023, 2023.
- 789 Levy, R. C., Mattoo, S., Munchak, L. A., Remer, L. A., Sayer, A. M., Patadia, F., and Hsu, N. C.:  
790 The Collection 6 MODIS aerosol products over land and ocean, *Atmospheric Measurement*  
791 *Techniques*, 6, 2989-3034, 10.5194/amt-6-2989-2013, 2013.
- 792 Liu, J., Alexander, L., Fast, J. D., Lindenmaier, R., and Shilling, J. E.: Aerosol characteristics at  
793 the Southern Great Plains site during the HI-SCALE campaign, *Atmospheric Chemistry*  
794 *and Physics*, 21, 5101-5116, 10.5194/acp-21-5101-2021, 2021.
- 795 Lohmann, U. and Feichter, J.: Global indirect aerosol effects: a review, *Atmospheric Chemistry*  
796 *and Physics*, 5, 715-737, 10.5194/acp-5-715-2005, 2005.
- 797 Lv, M., Wang, Z., Li, Z., Luo, T., Ferrare, R., Liu, D., Wu, D., Mao, J., Wan, B., Zhang, F., and  
798 Wang, Y.: Retrieval of Cloud Condensation Nuclei Number Concentration Profiles From  
799 Lidar Extinction and Backscatter Data, *Journal of Geophysical Research: Atmospheres*,  
800 123, 6082-6098, 10.1029/2017jd028102, 2018.
- 801 Mamouri, R.-E. and Ansmann, A.: Potential of polarization lidar to provide profiles of CCN- and  
802 INP-relevant aerosol parameters, *Atmospheric Chemistry and Physics*, 16, 5905-5931,  
803 10.5194/acp-16-5905-2016, 2016.
- 804 Müller, D., Ansmann, A., Mattis, I., Tesche, M., Wandinger, U., Althausen, D., and Pisani, G.:  
805 Aerosol-type-dependent lidar ratios observed with Raman lidar, *Journal of Geophysical*  
806 *Research: Atmospheres*, 112, 10.1029/2006jd008292, 2007.
- 807 Newsom, R., Sivaraman, C., & Zhang, D.: Water vapor mixing ratio from Raman Lidar.  
808 <https://doi.org/10.5439/1417037>, 2018a.
- 809 Newsom, R., Sivaraman, C., & Zhang, D.: Temperature profiles from Raman Lidar.  
810 <https://doi.org/10.5439/1417045>, 2018b.
- 811 Nicolae, D., Vasilescu, J., Talianu, C., Binietoglou, I., Nicolae, V., Andrei, S., and Antonescu, B.:  
812 A neural network aerosol-typing algorithm based on lidar data, *Atmospheric Chemistry*  
813 *and Physics*, 18, 14511-14537, 10.5194/acp-18-14511-2018, 2018.
- 814 Omar, A. H., Winker, D. M., Vaughan, M. A., Hu, Y., Trepte, C. R., Ferrare, R. A., Lee, K.-P.,  
815 Hostetler, C. A., Kittaka, C., Rogers, R. R., Kuehn, R. E., and Liu, Z.: The CALIPSO  
816 Automated Aerosol Classification and Lidar Ratio Selection Algorithm, *Journal of*  
817 *Atmospheric and Oceanic Technology*, 26, 1994-2014, 10.1175/2009jtecha1231.1, 2009.
- 818 Papagiannopoulos, N., Mona, L., Amodeo, A., D'Amico, G., Gumà Claramunt, P., Pappalardo, G.,  
819 Alados-Arboledas, L., Guerrero-Rascado, J. L., Amiridis, V., Kokkalis, P., Apituley, A.,  
820 Baars, H., Schwarz, A., Wandinger, U., Binietoglou, I., Nicolae, D., Bortoli, D., Comerón,  
821 A., Rodríguez-Gómez, A., Sicard, M., Papayannis, A., and Wiegner, M.: An automatic  
822 observation-based aerosol typing method for EARLINET, *Atmospheric Chemistry and*  
823 *Physics*, 18, 15879-15901, 10.5194/acp-18-15879-2018, 2018.
- 824 Pappalardo, G., Amodeo, A., Apituley, A., Comerón, A., Freudenthaler, V., Linné, H., Ansmann,  
825 A., Bösenberg, J., D'Amico, G., Mattis, I., Mona, L., Wandinger, U., Amiridis, V., Alados-  
826 Arboledas, L., Nicolae, D., and Wiegner, M.: EARLINET: towards an advanced  
827 sustainable European aerosol lidar network, *Atmospheric Measurement Techniques*, 7,  
828 2389-2409, 10.5194/amt-7-2389-2014, 2014.



- 829 Pedregosa, F., Varoquaux, G., Gramfort, A., Michel, V., Thirion, B., Grisel, O., Blondel, M.,  
830 Prettenhofer, P., Weiss, R., Dubourg, V., Vanderplas, J., Passos, A., Cournapeau, D.,  
831 Brucher, M., Perrot, M., and Duchesnay, E.: Scikit-learn: Machine learning in Python, *J.*  
832 *Mach. Learn. Res.*, **12**, 2825–2830, 2011.
- 833 Rosenfeld, D., Andreae, M. O., Asmi, A., Chin, M., De Leeuw, G., Donovan, D. P., Kahn, R.,  
834 Kinne, S., Kivekäs, N., Kulmala, M., Lau, W., Schmidt, K. S., Suni, T., Wagner, T., Wild,  
835 M., and Quaas, J.: Global observations of aerosol-cloud-precipitation-climate interactions,  
836 *Reviews of Geophysics*, **52**, 750–808, 10.1002/2013rg000441, 2014.
- 837 Rasmussen, C. E., and C. K. I. Williams (2006), *Gaussian Processes for Machine Learning*, 248  
838 pp., MIT Press, Cambridge, Mass.
- 839 Russell, P. B., Kacenelenbogen, M., Livingston, J. M., Hasekamp, O. P., Burton, S. P., Schuster,  
840 G. L., et al.: A multiparameter aerosol classification method and its application to retrievals  
841 from spaceborne polarimetry, *J. Geophys. Res.-Atmos.*, **119**, 9838–9863, 2014.
- 842 Seinfeld, J. H., Bretherton, C., Carslaw, K. S., Coe, H., DeMott, P. J., Dunlea, E. J., et al.:  
843 Improving our fundamental understanding of the role of aerosol–cloud interactions in the  
844 climate system, *Proc. Natl. Acad. Sci. USA*, **113**, 5781–5790, 2016.
- 845 Shinozuka, Y., Clarke, A. D., Nenes, A., Jefferson, A., Wood, R., Mcnaughton, C. S., Ström, J.,  
846 Tunved, P., Redemann, J., Thornhill, K. L., Moore, R. H., Latham, T. L., Lin, J. J., and  
847 Yoon, Y. J.: The relationship between cloud condensation nuclei (CCN) concentration and  
848 light extinction of dried particles: indications of underlying aerosol processes and  
849 implications for satellite-based CCN estimates, *Atmospheric Chemistry and Physics*, **15**,  
850 7585–7604, 10.5194/acp-15-7585-2015, 2015.
- 851 Sugimoto, N., Matsui, I., Shimizu, A., Uno, I., Asai, K., Endoh, T., and Nakajima, T.: Observation  
852 of dust and anthropogenic aerosol plumes in the Northwest Pacific with a two-wavelength  
853 polarization lidar on board the research vessel Mirai, *Geophysical Research Letters*, **29**, 7-  
854 1-7-4, 10.1029/2002gl015112, 2002.
- 855 Tackett, J. L., Kar, J., Vaughan, M. A., Getzewich, B. J., Kim, M.-H., Vernier, J.-P., Omar, A. H.,  
856 Magill, B. E., Pitts, M. C., and Winker, D. M.: The CALIPSO version 4.5 stratospheric  
857 aerosol subtyping algorithm, *Atmospheric Measurement Techniques*, **16**, 745–768,  
858 10.5194/amt-16-745-2023, 2023.
- 859 Thorsen, T. J., Q. Fu, R. K. Newsom, D. D. Turner, and J. M. Comstock, 2015a: Automated  
860 Retrieval of Cloud and Aerosol Properties from the ARM Raman Lidar. Part I: Feature  
861 Detection. *J. Atmos. Oceanic Technol.*, **32**, 1977–1998, <https://doi.org/10.1175/JTECH-D-14-00150.1>.
- 862  
863 Thorsen, T. J., and Q. Fu, 2015b: Automated Retrieval of Cloud and Aerosol Properties from the  
864 ARM Raman Lidar. Part II: Extinction. *J. Atmos. Oceanic Technol.*, **32**, 1999–2023,  
865 <https://doi.org/10.1175/JTECH-D-14-00178.1>.
- 866 Uin, J. and Enekwizu, O.: Cloud condensation nuclei particle counter (CCN) instrument handbook,  
867 *U.S. Department of Energy, Office of Science, Atmospheric Radiation Measurement (ARM)*  
868 *User Facility*, DOE/SC-ARM-TR-168, <https://doi.org/10.2172/1251411>, 2024.
- 869 Uin, J. and Mei, F.: *Cloud Condensation Nuclei Particle Counter Instrument Handbook – Airborne*  
870 *Version*, U.S. Department of Energy, <https://doi.org/10.2172/1562677>, 2019.
- 871 Veselovskii, I., Hu, Q., Goloub, P., Podvin, T., Barchunov, B., and Korenskii, M.: Combining Mie–  
872 Raman and fluorescence observations: a step forward in aerosol classification with lidar  
873 technology, *Atmospheric Measurement Techniques*, **15**, 4881–4900, 10.5194/amt-15-4881-  
874 2022, 2022.



- 875 Wandinger, U., Floutsi, A. A., Baars, H., Haarig, M., Ansmann, A., Hünerbein, A., Docter, N.,  
876 Donovan, D., Van Zadelhoff, G.-J., Mason, S., and Cole, J.: HETEAC – the Hybrid End-  
877 To-End Aerosol Classification model for EarthCARE, *Atmospheric Measurement*  
878 *Techniques*, 16, 2485-2510, 10.5194/amt-16-2485-2023, 2023.
- 879 Watson-Parris, D., Schutgens, N., Reddington, C., Pringle, K. J., Liu, D., Allan, J. D., Coe, H.,  
880 Carslaw, K. S., and Stier, P.: In situ constraints on the vertical distribution of global aerosol,  
881 *Atmospheric Chemistry and Physics*, 19, 11765-11790, 10.5194/acp-19-11765-2019,  
882 2019.
- 883 Zhang, D., Comstock, J., and Morris, V.: Comparison of planetary boundary layer height from  
884 ceilometer with ARM radiosonde data, 10.5194/amt-15-4735-2022, 2022.
- 885 Zieger, P., Fierz-Schmidhauser, R., Gysel, M., Ström, J., Henne, S., Yttri, K. E., Baltensperger, U.,  
886 and Weingartner, E.: Effects of relative humidity on aerosol light scattering in the Arctic,  
887 *Atmospheric Chemistry and Physics*, 10, 3875-3890, 10.5194/acp-10-3875-2010, 2010.